measurements on about 50 ships at various steady-state engine loads. A recent analysis[27] of *in situ* aircraft measurements of NO_x in the exhaust plumes of four slow-speed diesel ships indicates a range of 8.4–14 kg N per t fuel, about 0.33–0.5 times the value assumed above. It is unknown whether the discrepancy is due to problems with the techniques of NO_x emission measurement, or whether it is because only a very few ships could be considered in the latter study. Furthermore, it is uncertain how representative either of these emission factors can be for the current global fleet of over 100,000 registered vessels. Resolving these issues is critical for providing an accurate base of information for future policy decisions. In particular, extensive measurements in and around the main shipping routes are needed to obtain a picture of the influence of the ship NO_x source on the oceanic NO_x distribution and its further effect on O_3 and $OH^{\cdot}$ concentrations.

The effects of ocean-going ship emission of NO_x on the tropospheric oxidizing power that we calculate, and the potential for cooling effects, are expected to increase notably over the coming decades, as ship traffic is currently growing by about 3% yr^{-1} globally[9], and even more strongly in the tropics. The CO_2 release to the atmosphere from ships (120–150 Tg C yr^{-1}; ref. 9) is about 2–2.5% of the global release of CO_2 from fossil-fuel burning[28]. In comparison, the corresponding fractional release for SO_2 and NO_x are substantially larger, 5% for SO_2 and as much as 10–15% for NO_x (refs 9, 28). Thus there is good reason for considering policy measures aimed at reducing the relatively large pollutant emissions from ships, as initiated by the International Maritime Organization mainly for coastal regions[9]. However, reduced SO_2 emissions can decrease the Earth's albedo, while reduced NO emissions from ships lead to lower concentrations of $OH^{\cdot}$ over the open ocean, thereby enhancing the concentrations of the greenhouse-gas CH_4 and reducing the production rates of new aerosol particles. All three of these factors exert a warming effect on the Earth's climate, presenting policy makers with a striking dilemma. □

Methods

We use the Model of Atmospheric Transport and Chemistry, Max-Planck-Institute for Chemistry version[13] (MATCH-MPIC). The meteorology component of MATCH (ref. 14 and references therein) simulates advective transport, convection, vertical diffusion, cloud fractions and microphysics. The simulations are done 'semi-offline', that is, gridded values for basic meteorological parameters (pressure, temperature, horizontal winds, surface heat fluxes, and surface stresses) are read in from the NCEP/NCAR reanalysis project data[29]; the remaining meteorological properties (such as water vapour and cloud transport) are computed online.

The O_3–HO_x–NO_x–CH_4–CO tropospheric photochemistry version of MATCH-MPIC[13] simulates the following: surface sources of NO_x, CO and CH_4 (for example, industry, biomass burning); free tropospheric sources of NO_x (lightning, aircraft); the stratosphere-to-troposphere fluxes of O_3 and NO_y; photochemical and photolytic processes; surface deposition loss; heterogeneous loss of N_2O_5 on aerosols; and cloud scavenging by precipitation and settling processes. The runs start in December 1992, and are continued to the end of December 1993, allowing the first December as a 'spin-up' period to reduce dependence on the initial conditions (which are from ref. 13). The model version used here is an updated version of MATCH-MPIC 2.0 (described in ref. 13); the only notable change for the present study is that the EDGAR fossil-fuel NO_x emissions[4] (with ship emissions scaled up to 3 Tg N yr^{-1}) have replaced the previously used distribution[3].

Received 20 May; accepted 15 September 1999.

1. Kasibhatla, P. S., Levy, H. & Moxim, W. J. Global NO_x, HNO_3, PAN, and NO_y distributions from fossil fuel combustion emissions: A model study. *J. Geophys. Res.* **98,** 7165–7180 (1993).
2. Crutzen, P. J. & Zimmermann, P. H. The changing photochemistry of the troposphere. *Tellus* **43A–B,** 136–151 (1991).
3. Benkovitz, C. M. *et al.* Global gridded inventories of anthropogenic emissions of sulfur and nitrogen. *J. Geophys. Res.* **101,** 29239–29253 (1996).
4. Olivier, J. G. *et al. Description of EDGAR Version 2.0. A Set of Global Emission Inventories of Greenhouse Gases and Ozone-depleting Substances for all Anthropogenic and Most Natural Sources on a Per Country Basis and on 1° × 1° Grid* (Rep. no. 771060 002 RIVM (National Institute of Public Health and the Environment, Bilthoven, 1996).
5. Crutzen, P. J. & Andreae, M. O. Biomass burning in the tropics: Impact on atmospheric chemistry and biogeochemical cycles. *Science* **250,** 1669–1678 (1990).
6. Yienger, J. J. & Levy, H. Empirical model of global soil-biogenic NO_x emissions. *J. Geophys. Res.* **100,** 11447–11464 (1995).
7. Baughcum, S. L., Henderson, S. C., Hertel, P. S., Maggiora, D. R. & Oncina, C. A. *Stratospheric Emissions Effects Database Development* (CR-4592, NASA, Washington DC, 1994).
8. Lawrence, M. G., Chameides, W. L., Kasibhatla, P. S., Levy, H. & Moxim, W. in *Handbook of Atmospheric Electrodynamics* (ed. Volland, H.) 189–202 (CRC, Boca Raton, 1995).
9. Corbett, J. J., Fischbeck, P. S. & Pandis, S. N. Global nitrogen and sulfur inventories for oceangoing ships. *J. Geophys. Res.* **104,** 3457–3470 (1999).
10. Carlton, J. S. *et al. Marine Exhaust Emissions Research Programme* (Lloyd's Register Engineering Services, London, 1995).
11. *Dataset of Ships 100 GRT or Greater* (Lloyd's Maritime Information Services, Stamford, Connecticut, 1996).
12. Malony, M. J. *World Energy Database* (Energy Information Administration (EIA), Washington DC, 1996).
13. Lawrence, M. G., Crutzen, P. J., Rasch, P. J., Eaton, B. E. & Mahowald, N. M. A model for studies of tropospheric photochemistry: Description, global distributions, and evaluation. *J. Geophys. Res.* (in the press).
14. Rasch, P. J., Mahowald, N. M. & Eaton, B E. Representations of transport, convection, and the hydrologic cycle in chemical transport models: Implications for the modeling of short lived and soluble species. *J. Geophys. Res.* **102,** 28127–28138 (1997).
15. *The Times Atlas of the World Comprehensive Edition* 9th edn (Times Books, London, 1992).
16. International Maritime Organization (IMO) *IMO Sub-Committee on Bulk Materials, 22nd Session, Agenda Item 7* (Ref. code IMO, BCH 22/INF.10, International Maritime Organization, London, 1992).
17. Houweling, S., Dentener, F. & Lelieveld, J. The impact of nonmethane hydrocarbon compounds on tropospheric photochemistry. *J. Geophys. Res.* **103,** 10673–10696 (1998).
18. Sander, R. & Crutzen, P. J. Model study indicating halogen activation and ozone destruction in polluted air masses transported to the sea. *J. Geophys. Res.* **101,** 9121–9138 (1996).
19. Liu, S. C. *et al.* Ozone production in the rural troposphere and the implications for regional and global ozone distributions. *J. Geophys. Res.* **92,** 4191–4207 (1987).
20. Gerbig, C. *et al.* Fast response resonance fluorescence CO measurements aboard the C-130: Instrument characterization and measurements made during North Atlantic Regional Experiment 1993. *J. Geophys. Res.* **101,** 29229–29238 (1996).
21. Emmons, L. K. *et al.* Climatologies of NO_x and NO_y: A comparison of data and models. *Atmos. Environ.* **31,** 1851–1904 (1997).
22. Prinn, R. G. *et al.* Atmospheric trends and lifetime of CH_3CCL_3 and global OH concentrations. *Science* **269,** 187–192 (1995).
23. Krol, M., van Leeuwen, P. J. & Lelieveld, J. Global OH trend inferred from methylchloroform measurements. *J. Geophys. Res.* **103,** 10697–10711 (1998).
24. DeMore, W. B. *et al. Chemical Kinetics and Photochemical Data for Use in Stratospheric Modeling* (NASA JPL (Jet Propulsion Laboratory), Pasadena, California, 1997).
25. Raes, F. Entrainment of free tropospheric aerosols as a regulating mechanism for cloud condensation nuclei in the remote marine boundary layer. *J. Geophys. Res.* **100,** 2893–2903 (1995).
26. Capaldo, K., Corbett, J. J., Kasibhatla, P., Fischbeck, P. & Pandis, S. N. Effects of ship emissions on sulphur cycling and radiative climate forcing over the ocean. *Nature* **400,** 743–746 (1999).
27. Hobbs, P. V. *et al.* Emissions from ships with respect to their effects on clouds. *J. Atmos. Sci.* (in the press).
28. Houghton, J. T. *et al.* (eds) *Climate Change 1994* (Cambridge Univ. Press, 1995).
29. Kalnay, E. *et al.* The NCEP/NCAR 40-year reanalysis project. *Bull. Am. Met. Soc.* **77,** 437–471 (1996).

Acknowledgements

We thank P. Rasch and B. Eaton for MATCH support, and J. Olivier for information on the EDGAR ship emissions dataset. This work was supported by the EU SINDICATE project.

Correspondence and requests for materials should be addressed to M.G.L. (e-mail: lawrence@mpch-mainz.mpg.de).

A polar vortex in the Earth's core

Peter Olson & Jonathan Aurnou

Department of Earth and Planetary Sciences, Johns Hopkins University, Baltimore, Maryland 21218, USA

Numerical dynamo models have been successful in explaining the origin of the Earth's magnetic field and its secular variation by convection in the electrically conducting fluid outer core[1–7]. An important component of the convection in the numerical dynamos are polar vortices beneath the core–mantle boundary in each hemisphere. These polar vortices in the outer core have been proposed as sources for both the anomalous rotation of the inner core and the toroidal part of the geomagnetic field[2,8]. Here we use the observed structure of the Earth's magnetic field and its variation since 1870 to infer the existence of an anticyclonic polar vortex with a polar upwelling in the northern hemisphere of the core, consistent with the polar vortices found in numerical dynamos.

The Earth's solid inner core has an important effect on the pattern

of convection in the liquid outer core and on the geomagnetic field, according to dynamo theory. Because the convection is expected to be quasi-geostrophic and nearly two-dimensional, the outer core is divided into two regions, separated by the tangent cylinder, an imaginary cylinder tangent to the inner-core equator and parallel to the Earth's rotation axis. Inside the tangent cylinder, convection-driven dynamos show intense polar vortices associated with upwellings or downwellings in both the northern and southern hemispheres. Convective upwellings that generate anticyclonic polar-vortex motion beneath the core–mantle boundary (CMB) seem to be preferred[1,2,5,6], but downwellings with cyclonic polar-vortex motion beneath the CMB are seen in some numerical dynamos[3].

The geomagnetic field and its secular variation can be used to map the flow in the outer core beneath the CMB. Because of high electrical conductivity in the core, advection of the magnetic field by the flow dominates over diffusion and the magnetic flux lines tend to move with the fluid. This 'frozen flux' property has been used previously to construct global maps of the large-scale core flow[9–14]. Here we use the same basic technique to delineate a more localized flow structure: a polar vortex.

Figures 1a and c show maps of the radial component of the geomagnetic field on the CMB at epochs 1870 and 1990, respectively[15]. The effect of an anticyclonic vortex can be seen in the change in field structure with time in the north polar region. Anticyclonic motion inside the tangent cylinder is evident from the clockwise motion of the patch of reversed magnetic flux during the 120-year interval. The boundary of this patch (the curve along which the radial flux is zero) represents a material curve in a hypothetical perfectly conducting core[16]. Although the core is not a perfect conductor, its conductivity is high enough that the westward rotation of the patch about the north pole implies anticyclonic flow just below the CMB. A simple cross-correlation of the fields at the two epochs indicates anticyclonic motion inside the tangent cylinder, with an average angular speed of about 0.25° per year.

Evidence for a generally southward meridional flow inside the tangent cylinder comes from the change in energy density of the polar magnetic field with time. Although the geomagnetic field is largely an axial dipole on the Earth's surface, the radial component of the field on the CMB is maximum not at the pole, as for an axial dipole, but instead at two flux bundles located just outside the tangent-cylinder region[17], as shown in Fig. 1a and c. There is a minimum in intensity of the axisymmetric part of the field at the pole, and a maximum just outside the tangent cylinder. During this time period, the azimuthally averaged magnetic-energy density close to the pole tends toward zero, while the energy density near the tangent cylinder increases, as shown in Fig. 1b. This behaviour indicates that magnetic flux is being expelled from the polar region and concentrated at lower latitudes. The flux expulsion suggests a polar upwelling and southward meridional flow, which transports the field lines away from the pole and towards the tangent cylinder.

The axisymmetric part of the vortex is determined by inverting the radial component of the magnetic induction equation in the

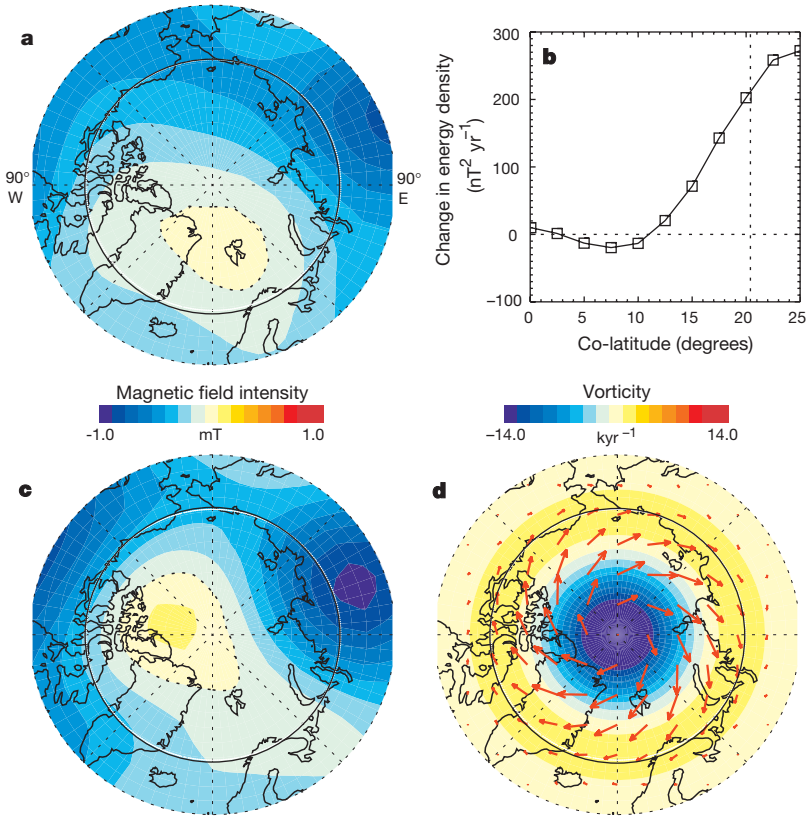

Figure 1 Secular variation of the geomagnetic field observed over the north-polar region of the core–mantle boundary and structure of the inferred axisymmetric polar vortex in the outer core. The continental outlines and the inner-core tangent-cylinder radius are shown for reference in **a**, **c** and **d**. **a**, **c**, Contours of the radial component of the geomagnetic field intensity on the core–mantle boundary in millitesla at epochs 1870 (**a**) and 1990 (**c**) from the geomagnetic field model of Bloxham and Jackson[15]. The westward motion of the null flux curve (dashed contours) shows the direction of fluid motion in the anticyclonic vortex. **b**, Change in the energy density of the radial component of the magnetic field on the core–mantle boundary, in nanotesla squared per year, during 1870–1990. The energy decrease near the pole and the corresponding energy increase near the inner-core radius (dashed line near co-latitude 20.4°) imply magnetic-flux expulsion by a north-polar upwelling and generally southward meridional flow. **d**, Inferred axisymmetric structure of the north-polar vortex. Arrows indicate tangential velocities (maximum 0.13 mm s^{-1}) and colour contours indicate vorticity.

frozen-flux (high magnetic Reynolds number) limit:

$$\frac{\partial B_r}{\partial t} + \nabla_H \cdot (B_r \mathbf{U_H}) = 0 \qquad (1)$$

For B_r, the radial component of the geomagnetic field, we use the time-average field on the CMB from 1870–1990 (ref. 15) and we use the difference between the fields at 1990 and 1870 to compute the secular variation $\partial B_r/\partial t$. We then solve equation (1) for $\mathbf{U}_H$, the velocity field in the outer core, tangent to the CMB (the subscript H denotes tangential coordinates.) We restrict our attention to the axisymmetric part of the flow, assumed to be steady over the time interval of the calculation. This allows us to solve for the two components of the tangential velocity without making additional assumptions. The surface integral of the axisymmetric part of equation (1) yields the meridional velocity U_θ directly. The non-axisymmetric part of equation (1) is then inverted using the least-squares method for the azimuthal velocity U_ϕ (here θ denotes co-latitude and ϕ denotes east longitude).

Figures 1d, 2 and 3 show the axisymmetric flow in the northern hemisphere found with this procedure. The azimuthal flow is anticyclonic everywhere and is concentrated inside the tangent cylinder. Its maximum angular speed corresponds to a westward drift rate of about 0.6° per year. The 120-year average westward drift rate inside the tangent cylinder is 0.25° per year, almost four times greater than the global average value over the same time period (see Fig. 3). Figure 2c and d shows the axisymmetric distributions of meridional velocity and vorticity. The vorticity is negative within 15° of the pole, but becomes positive at lower latitudes, reaching a local maximum around the tangent cylinder. The vorticity reversal has the effect of confining the azimuthal circulation to the region inside the tangent cylinder, shielding the polar vortex from the rest of the core circulation. The axisymmetric meridional flow is southward inside the tangent cylinder, but becomes northward beyond the tangent cylinder. The arrows in Fig. 2c indicate the regions of upwelling and downwelling implied by the divergence of the meridional flow. The region of implied upwelling is confined to the vortex core, within about 10° of the pole. Elsewhere the meridional flow is convergent and the implied radial motion is downwelling.

The profiles of the azimuthal velocity, meridional velocity, vorticity and angular velocity shown in Fig. 2 are similar in shape to baroclinic, convection-driven polar vortices in the numerical dynamo calculations[2,5,6]. These profiles are also qualitatively similar to isolated vortices generated in rotating fluids[18] in the laboratory and, apart from the difference in sign, are broadly similar to the structure of the polar vortices in the stratosphere[19] and to the convective chimneys in the deep ocean[20]. The intensity of the polar vortices in the numerical dynamos tends to be larger than in Fig. 2, depending on the parameters of the calculation. But the core vortex could be stronger than our frozen-flux method indicates. When we apply our technique to the dynamo models, we recover the shapes of the polar vortices but underestimate their intensity. This is because a significant part of the flow in the dynamo models is parallel to the magnetic field contours and does not contribute to the secular variation of the field[21]. The same situation could occur in the Earth's core. We could add an arbitrary amount of motion parallel to the contour lines in Fig. 1a and c, which would not be detected using the frozen-flux technique.

Because the vortex occupies a small portion of the CMB, it is near the limit of resolution of current geomagnetic field models and near the limit of validity of the frozen-flux assumption. Accordingly, it is important to determine how robust the results are with respect to variations in model parameters. Figure 3 shows the sensitivity of the average westward drift in the vortex to variations in the epoch and window length since 1870, the year which marks the advent of polar data in the geomagnetic field model[15]. Figure 3 indicates that the anticyclonic motion is a persistent feature in the field model since 1870, at all epochs and for all window lengths. The shortest time windows produce a cosine fluctuation in westward drift about the 120-year average, with a period of about 80 years and a minimum near epoch 1920. Longer windows systematically approach the 120-year average. We have also calculated the axisymmetric polar flow using this geomagnetic field model truncated at spherical harmonic degree 4, the twentieth-century degree-4 field model of Yokoyama and Yukutake[22], and a degree-4 archeomagnetic field model (Y. Hamano, personal communication). All three lower-resolution models show westward flow in the northern tangent cylinder.

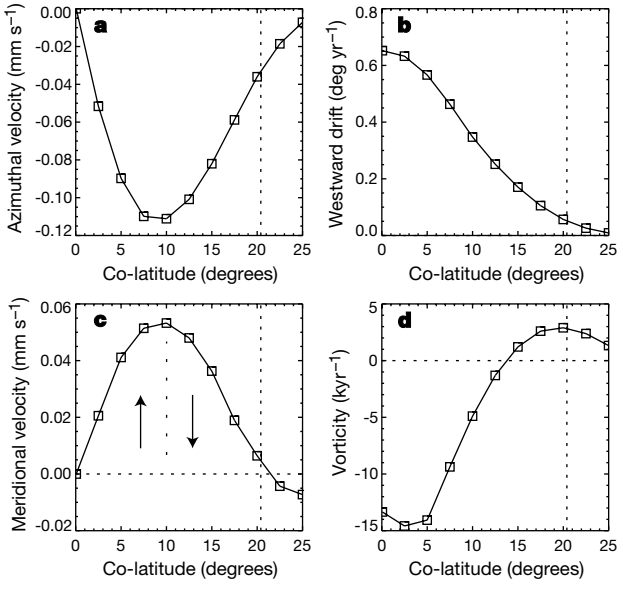

Figure 2 Profiles of the axisymmetric flow versus co-latitude in the inferred north-polar vortex 1870–1990. **a**, Azimuthal velocity (negative values are westward); **b**, angular velocity expressed as westward drift; **c**, meridional velocity (positve values are southward); **d**, vorticity (curl of the azimuthal velocity). The regions with inferred upwelling and downwelling are indicated by the arrows in **c**. Dashed lines at 20.4° indicate the co-latitude of the inner-core tangent cylinder.

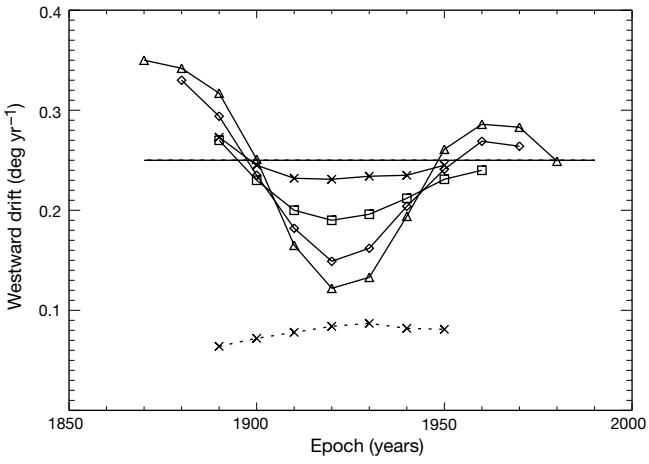

Figure 3 Persistence of the north polar vortex since 1870, determined using different time windows of geomagnetic secular variation. Solid curves show the average angular velocity inside the inner-core tangent cylinder, expressed as westward drift rate in degrees per year relative to the crust and mantle. The symbols indicate the midpoint in time (epoch) of the different time windows used: triangles, 20 years; diamonds, 40 years; squares, 60 years; crosses, 80 years. The horizontal solid line is the value for 1870–1990 from the average of Fig. 2b, obtained from the data in Fig. 1. The dotted curve shows the average drift rate over the entire core–mantle boundary.

In another test, we compare the observed and predicted geomagnetic secular variation, obtained by integrating the finite difference version of equation (1) forward in time using the velocities in Fig. 2a and c, and the 1870 field as the initial condition. A small amount of tangential diffusion was included to stabilize these calculations. The results are insensitive to diffusion for magnetic diffusivities less than 30 $m^2 s^{-1}$ (about ten times the value estimated for the outer core[23], which supports use of the frozen-flux approximation for the axisymmetric part of the flow). The misfit between the calculated and the observed secular variation, measured using the parameter σ of Voorhies[10], varies with time from ~0.3 to 0.5 during the 120-year interval. Overall, the axisymmetric vortex accounts for about 60% of the variance in the tangent cylinder field during this time. Nearly all of the unexplained secular variation comes from localized intensification of two features—the reversed flux patch inside the tangent cylinder and the normal-polarity flux patch beneath Siberia. The field intensification within these patches violates the frozen-flux constraint. It indicates the presence of convection on scales smaller than the field-model resolution and radial magnetic diffusion in these regions.

A frozen-flux analysis of the geomagnetic field near the south pole shows some evidence for flux expulsion there. But we do not find evidence of coherent vortex motion in the southern-hemisphere tangent cylinder. Differences in magnetic field behaviour between the polar regions might simply be an artefact of poorer data coverage near the south pole before the first decades of this century. Alternatively, it might reflect genuine differences in the flow pattern of the two regions, isolated from each other by the solid inner core.

Our results differ from most global models of the core flow. Some global models do show retrograde azimuthal motion inside the northern tangent cylinder[9–14], but without the large angular-velocity concentration that we find. This difference might be due to model resolution: global models use spherical harmonics and tend to fit the secular variation at low and middle latitudes, whereas our method treats only the polar region. The only exception is the Pais and Hulot global model[11], which focuses on the axisymmetric azimuthal part of the flow. They obtain an azimuthal flow pattern similar to Fig. 2 with a distinct polar vortex, but with larger amplitude. However, they attribute the vortex to a particular zonal spherical harmonic of the flow—degree 7—implying a similar vortex near the south pole, for which we do not find evidence.

Anticyclonic polar vorticity near the CMB has implications for the structure of convection deeper in the core. Some studies using seismic body waves have inferred anomalous prograde inner-core rotation[24,25], while other studies based on normal modes find no anomalous inner-core rotation relative to the crust and mantle[26]. Either result indicates that the anticyclone weakens or possibly reverses direction somewhere between the CMB and the inner core. Previously the westward geomagnetic drift has been interpreted in terms of either cylindrically symmetric[12] or spherically symmetric[27] flow. Our results indicate that the convection in the north polar region has a structure more like a tropical hurricane[28], cylindrical in shape with circulation and vorticity changing with depth through the outer core. □

Received 30 April; accepted 28 September 1999.

1. Glatzmaier, G. A. & Roberts, P. H. A three-dimensional self-consistent computer simulation of a geomagnetic reversal. *Nature* **377,** 203–208 (1995).
2. Glatzmaier, G. A. & Roberts, P. H. Rotation and magnetism of Earth's inner core. *Science* **274,** 1887–1891 (1996).
3. Kuang, W. & Bloxham, J. An Earth-like numerical dynamo model. *Nature* **389,** 371–374 (1997).
4. Busse, F. H., Grote, E. & Tilgner, A. On convection driven dynamos in rotating spherical shells. *Stud. Geophys. Geodaet.* **42,** 1–6 (1998).
5. Olson, P., Christensen, U. & Glatzmaier, G. A. Numerical modeling of the geodynamo: Mechanisms of field generation and equilibration. *J. Geophys. Res.* **104,** 10383–10404 (1999).
6. Christensen, U., Olson, P. & Glatzmaier, G. A. Numerical modeling of the geodynamo; a systematic parameter study. *Geophys. J. Int.* **138,** 393–409 (1999).
7. Glatzmaier, G. A., Coe, R. S., Longre, L & Roberts, P. H. The role of the Earth's mantle in controlling the frequency of geomagnetic reversals. *Nature* (in the press).
8. Aurnou, J. M., Brito, D. & Olson, P. L. Mechanics of inner core super-rotation. *Geophys. Res. Lett.* **23,** 3401–3404 (1996).
9. Voorhies, C. V. Steady flows at the top of Earth's core derived from geomagnetic field models. *J. Geophys. Res.* **91,** 12444–12466 (1986).
10. Voorhies, C. V. Time-varying flows at the top of Earth's core derived from definitive geomagnetic reference models. *J. Geophys. Res.* **100,** 10029–10039 (1995).
11. Pais, A. & Hulot, G. Core surface zonal flows, length of day decade variations and inner core superrotation. *Phys. Earth Planet. Inter.* (submitted).
12. Jault, D., Gire, C. & LeMouel, J.-L. Westward drift, core motions and exchanges of angular momentum between core and mantle. *Nature* **333,** 353–356 (1988).
13. Bloxham, J. The steady part of the secular variation of the Earth's magnetic field. *J. Geophys. Res.* **97,** 19565–19579 (1992).
14. Jackson, A. Time-dependency of tangentially geostrophic core surface motions. *Phys. Earth Planet. Inter.* **103,** 293–311 (1997).
15. Bloxham, J. & Jackson, A. Time-dependent mapping of the geomagnetic field at the core-mantle boundary. *J. Geophys. Res.* **97,** 19357–19564 (1992).
16. Backus, G. E. Kinematics of the secular variation in a perfectly conducting core. *Phil. Trans. R. Soc. Lond. A* **263,** 239–266 (1968).
17. Gubbins, D. & Bloxham, J. Morphology of the geomagnetic field and implications for the geodynamo. *Nature* **325,** 509–511 (1987).
18. Hopfinger, E. J. & Van Heijst, G. J. F. Vortices in rotating fluids. *Annu. Rev. Fluid Mech.* **25,** 241–289 (1993).
19. Schloeberl, M. R. & Hartmann, D. L. The dynamics of the stratospheric polar vortex and its relation to springtime ozone depletions. *Science* **251,** 46–52 (1991).
20. Jones, H. & Marshall, J. Convection with rotation in a neutral ocean: a study of open-ocean deep convection. *J. Phys. Oceanogr.* **23,** 1009–1039 (1993).
21. Rau, S., Christensen, U., Jackson, A. & Wicht, J. Core flow inversion tested with numerical dynamo models. *Geophys. J. Int.* (submitted).
22. Yokoyama, Y. & Yukutake, T. Sixty year variation in a time series of the geomagnetic Gauss coefficients. *J. Geomagn. Geoelectr.* **43,** 563–584 (1997).
23. Stacey, F. D. *Physics of the Earth* (Brookfield, Brisbane, Australia, 1992).
24. Song, X. & Richards, P. G. Seismological evidence for the differential rotation of the Earth's inner core. *Nature* **382,** 221–224 (1996).
25. Creager, K. C. Inner core rotation rate from small-scale heterogeneity and time-varying travel times. *Science* **287,** 1284–1288 (1997).
26. Laske, G. & Masters, G. Limits on differential rotation of the inner core from an analysis of the Earth's free oscillations. *Nature* **402,** 66–69 (1999).
27. Voorhies, C. V. Inner core rotation from geomagnetic westward drift and a stationary spherical vortex in Earth's core. *Phys. Earth Planet. Inter.* **112,** 111–124 (1999).
28. Wu, C.-C. & Emanuel, K. E. Interaction of a baroclinic vortex with background shear: application to hurricane movement. *J. Atmos. Sci.* **50,** 62–76 (1993).

Acknowledgements

We thank J. Bloxham, Y. Hamano, and Y. Yokoyamo for providing the geomagnetic field models and D. Waugh for pointing out similarities with other geophysical vortices. A. Pais, G. Hulot, G. Laske and G. Masters kindly shared their results in advance of publication.

Correspondence and requests for materials should be addressed to P.O. (e-mail: olson@gibbs.eps.jhu.edu).

The insidious effect of diatoms on copepod reproduction

A. Miralto*, G. Barone†, G. Romano*, S. A. Poulet‡, A. Ianora*, G. L. Russo§, I. Buttino*, G. Mazzarella§, M. Laabir*, M. Cabrini‖ & M. G. Giacobbe¶

** Stazione Zoologica "A. Dohrn", Villa Comunale, 80121 Naples, Italy*
† Dipartimento di Chimica Organica e Biologica, Università di Napoli "Federico II", Via Mezzocannone 16, 80134 Naples, Italy
‡ Station Biologique de Roscoff, CNRS, Place Georges Teissier, 29682 Roscoff, France
§ Istituto di Scienze dell'Alimentazione, CNR, 83100 Avellino, Italy
‖ Laboratorio di Biologia Marina, Via August Piccard 54, 34040 Trieste, Italy
¶ Istituto Sperimentale Talassografico CNR, Via San Ranieri 86, 98122 Messina, Italy

The productive regions of the ocean are characterized by seasonal blooms of phytoplankton which are generally dominated by diatoms. This algal class has, therefore, traditionally been regarded as providing the bulk of the food that sustains the marine food chain to top consumers and important fisheries. However, this beneficial role has recently been questioned on the